

# Electrocatalysis by Co-Cu-W Mixed-metal Oxides: Insights from X-ray Absorption Spectroscopy

Nikita Gupta<sup>1,2</sup>, Carlo Segre<sup>3</sup>, Carsten Streb<sup>4</sup>, Dandan Gao<sup>4\*</sup>, Ksenija D. Glusac<sup>1,2\*</sup>

<sup>1</sup> Department of Chemistry, University of Illinois Chicago, Chicago, Illinois 60607, United States

<sup>2</sup> Chemical Sciences and Engineering, Argonne National Laboratory, Illinois 60439, United States

<sup>3</sup> Department of Physics, Center for Synchrotron Radiation Research and Instrumentation, Illinois Institute of Technology, Chicago, Illinois 60616, United States

<sup>4</sup> Department of Chemistry, Johannes Gutenberg University Mainz, Mainz 55128, Germany

**KEYWORDS** : *electrocatalysis · mixed metal oxide · real active species · X-ray absorption spectroscopy · water-splitting.*

---

**ABSTRACT:** Mixed metal oxides (MMOs) are a promising class of electrocatalysts for oxygen evolution (OER) and hydrogen evolution reactions (HER). Yet, our understanding of relevant reaction pathways, catalytically active sites and synergistic effects is quite limited. Here, we applied synchrotron-based X-ray absorption spectroscopy (XAS) to explore the evolution of a Co-Cu-W MMO electrocatalyst, shown previously to be an efficient bifunctional catalyst for water splitting. Ex-situ K- and L-edge XAS measurements provided structural environments and the oxidation state of the metals involved, revealing Co<sup>2+</sup> (octahedral), Cu<sup>+/2+</sup> (tetrahedral / square planar) and W<sup>6+</sup> (octahedral) centers. Meanwhile, the in-situ XAS investigations, including X-ray absorption near-edge structure (XANES) and extended X-ray absorption fine structure (EXAFS), elucidated the dynamic structural transformations of Co, Cu, and W metal centers during OER and HER. The experimental results indicate that Co<sup>3+</sup> and Cu<sup>+</sup> are the active catalytic sites involved in OER and HER, respectively, while Cu<sup>2+</sup> and W<sup>6+</sup> play crucial roles as structure stabilizers, suggesting strong synergistic interactions within the Co-Cu-W MMO system. These results, combined with the Tafel slope analysis, revealed that the bottleneck intermediate during OER is Co(III) hydroperoxide, whose formation is accompanied with the changes in the Cu-O bond lengths, pinpointing to a possible synergistic effects between Co and Cu ions. Our study highlighted important structural effects taking place during MMOs electrocatalysis and provided essential experimental insights into the complex catalytic mechanism of emerging MMOs electrocatalysts for advanced water splitting.

---

## INTRODUCTION

Green hydrogen is seen as a promising alternative to carbon-based fuels for use in various energy systems, including combustion engines, turbines, and fuel cells.<sup>1,2</sup> It is produced via water electrolysis, a process that can be expressed in terms of the two half-reactions, namely oxygen evolution reaction (OER) and hydrogen-evolution reaction (HER). OER is considered as the bottleneck of this process and usually requires high overpotentials. The sluggish OER kinetics arise due to challenges associated with the formation of a weak O-O bond and the orchestrating of four proton-coupled electron transfer steps at the desired potential. Traditionally, precious metal oxide (MO) catalysts, such as RuO<sub>2</sub> and IrO<sub>2</sub>, are applied as the benchmark OER catalysts with high catalytic activity. However, the high cost and scarcity in nature significantly limit their widespread use.<sup>3</sup> As a result, researchers are exploring the use of earth-abundant MOs composed of first-row transition metals, such as Co, Mn, Ni or Fe, as promising alternatives.<sup>4-7</sup> Remarkably, these non-noble MOs often perform better as mixed metal oxides (MMOs), where synergetic effects are able to boost the catalytic activity for both OER and HER.<sup>8-13</sup> For example, the Qiao group showed that the presence of Zn and Ni enhances the HER activity of CoO, by providing an ideal environment for intermediate H-binding (Ni<sup>2+</sup>) and by boosting the electrical conduction (Zn<sup>2+</sup>).<sup>14</sup> In another example, the Nocera group has

shown that the incorporation of Fe<sup>3+</sup> into the nickel oxide (NiO) matrix increases the ability of the catalyst to access Ni<sup>4+</sup> state, thus enhancing the OER performance.<sup>11</sup> Furthermore, the employment of MMOs as bifunctional catalysts also has the potential to simplify the catalyst design and fabrication, reduce cross-contamination, and prevent catalyst poisoning, making it an attractive option for the production of green hydrogen.

A comprehensive understanding of the catalytic mechanism of MMOs for OER and HER is being actively explored. Based on computational works, the OER in an alkaline medium is generally considered to occur via one of the two mechanistic pathways.<sup>28-31</sup> Pathway I, known as the adsorbate evolution mechanism, involves a single active site, in which the activity is strongly correlated with the adsorption energies of the M-O intermediates. This pathway includes the formation of adsorbed M-OH species on the catalyst surface, their subsequent transformation to M-OOH, and the eventual release of O<sub>2</sub>.<sup>32-34</sup> While pathway II, known as the lattice oxygen evolution mechanism, involves the participation of lattice oxygen in the oxide catalyst during O-O coupling and OER<sup>35,36</sup>. This pathway includes the direct combination of two M-O species, leading to O<sub>2</sub> formation and the generation of active species. Similarly, the HER can occur via one of two reaction pathways, both of which involve electrochemical hydrogen adsorption as the first step in the catalytic reaction. In this context, pathway I proceeds via an

electrochemical desorption step, which is known as the Volmer-Heyrovsky mechanism. While pathway II, known as the Volmer-Tafel mechanism, proceeds via a recombination reaction.<sup>36,37</sup> These mechanisms are analogous to the adsorbate evolution mechanism and lattice oxygen evolution mechanism in the case of OER, respectively. Furthermore, various descriptors have been proposed in the literature to correlate OER and HER activity, including the bond strengths of the bound M-OH and M-O intermediates,<sup>38-41</sup> exchange current density,<sup>42-44</sup> the count of 3d electrons in the metal ion,<sup>41,45,46</sup> number of unsaturated sites<sup>47,48</sup>, or the energy gap between O p-band relative to the Fermi level<sup>49</sup>. The use of descriptors greatly simplifies the understanding of metal oxide activity trends.

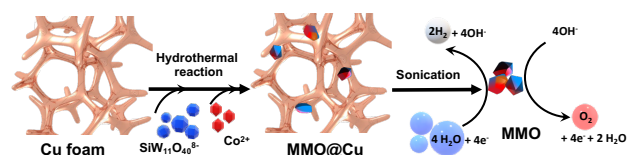
Additionally, the precise identification of catalytically active sites of MMOs electrocatalysts is also attracting substantial attention. In this regard, ex-situ characterization techniques can provide information regarding the atomic and electronic structures of the electrocatalyst pre- and post- catalytic OER / HER, while the in-situ investigation can shed light on the dynamic evolution of focused active sites over the catalytic process.<sup>50,51</sup> For example, several different in-situ characterization techniques have been used to study OER processes, such as surface interrogation-scanning electrochemical microscopy (SI-SECM),<sup>52</sup> transmission electron microscopy (TEM),<sup>53,54</sup> Raman spectroscopy,<sup>31,55</sup> Fourier transform infrared spectroscopy (FTIR),<sup>56</sup> X-ray diffraction (XRD),<sup>57-59</sup> ambient pressure X-ray photoelectron spectroscopy (APXPS),<sup>60</sup> Fe Mössbauer spectroscopy,<sup>61</sup> and electrochemical quartz crystal balance (EQCM).<sup>62-64</sup> In comparison to these techniques, X-ray absorption spectroscopy coupled with electrochemistry (XAS-EC) offers unique advantages in probing the chemical, electronic, and structural information of electrocatalysts. With XAS-EC, oxidation states, coordination environments, bond strengths, and catalytic intermediates of adsorbed atoms on active species can be studied to gain real-time insight into molecule-based catalytic mechanisms under operating conditions.<sup>31,59,65-67</sup> In one instructive example, studies by the Abruna group identified the active sites as  $\text{Co}^{2+/3+}$  and  $\text{Mn}^{2+/3+/4+}$  redox couples for a bimetallic  $\text{Co}_{1.5}\text{Mn}_{1.5}\text{O}_4/\text{C}$  catalyst system for OER and commented on the synergistic effect of Mn and Co.<sup>68</sup> In another example, the Boettcher group revealed the partial Fe oxidation and a shortened Fe-O bond length during OER on the synthesized  $\text{Co}(\text{Fe})\text{O}_x\text{H}_y$  electrocatalyst, while only Co oxidation was observed in the absence of Fe cation, indicative of the essential role of Fe cation for OER.<sup>69</sup>

In this study, we delve into the structural dynamics of a versatile bifunctional electrocatalyst developed by the Streb group,<sup>27</sup> specifically the Co-Cu-W mixed metal oxide (Co-Cu-W MMO) electrocatalyst that was formed by the hydrothermal reaction involving Co-ions, Cu-foam and polyoxometalate precursors (Scheme 1). The obtained Co-Cu-W MMO was found to be outstanding electrocatalyst for both OER and HER, with stable activity over prolonged time of more than 10 h. Furthermore, the electrocatalysis was highly efficient, with overpotentials of only 0.3 V and 0.1 V for OER and HER, respectively. However, the mechanism of electrocatalysis by Co-Cu-W MMO remains unexplored.

Here, employing cutting-edge XAS-EC at the Co and Cu K edges, as well as W L edge, we uncover the intriguing structural transformations of this MMO that occurs during water splitting. Through X-ray absorption near-edge structure (XANES), we gain precise knowledge regarding the oxidation states of the

constituent metals, while extended X-ray absorption fine structure (EXAFS) unveils the structural changes of each metal center over electrocatalysis. By combining Tafel slope analysis to derive information regarding the rate-determining step, we bring forward plausible mechanisms for catalysis by the Co-Cu-W MMO. The OER was found to predominantly occur at the Co-center, generating  $\text{Co}^{\text{III}}\text{-OOH}$  as a bottleneck intermediate that undergoes a rate-determining release of molecular oxygen. Importantly, we have also identified interesting structural changes that take place at the neighboring Cu-centers. While Cu does not undergo a change in the oxidation state, we discovered a lengthening of Cu-O bonds neighboring  $\text{Co}^{\text{III}}\text{-OOH}$  intermediate, and this result points to a possible synergistic role of the Cu-atoms to stabilize  $\text{Co}^{\text{III}}\text{-OOH}$  intermediate. These results shed light on the likely mechanism by which the Co-Cu-W MMO achieves such excellent OER performance and provide target catalytic motifs for future molecular engineering of bimetallic electrocatalysts. Under cathodic HER conditions, our Cu K-edge XAS-EC results provide strong evidence for the formation of  $\text{Cu}^0$  nanoparticles (NPs) with diameter increasing with electrolysis time to a value of 9 Å.

### SCHEME 1. Hydrothermal synthesis of Co-Cu-W MMO.



## RESULTS AND DISCUSSION

**Ex-situ XAS:** To comprehensively investigate the oxidation states and coordination environments of Co, W and Cu elements in the MMO, ex-situ XANES and EXAFS were performed. In this regard, two model polyoxometalates (POM) were synthesized as references: POM1 ( $\text{Na}_{10}[\text{Co}_4(\text{H}_2\text{O})_2(\text{PW}_9\text{O}_{34})_2]$ , Figure 1a) containing  $\text{Co}^{2+}$  and  $\text{W}^{6+}$  and POM2 ( $\text{Na}_5[\text{CoW}_{12}\text{O}_{40}]$ , Figure 1b) containing  $\text{Co}^{3+}$  and  $\text{W}^{6+}$ . Synthetic routes and characterization details, see supporting information (SI) and Figure S1. As shown in Figure 1c, the ex-situ Co K edge XANES spectra of POM1 demonstrate weak pre-edge features at 7710.6 eV and an edge energy of 7719 eV. Additionally, the pronounced white line characteristic implies a octahedral (Oh) coordination arrangement of the Co ions in POM1.<sup>69</sup> In contrast, POM2 exhibits distinct spectral features with a strong pre-edge peak (i: 7710.5 eV, assigned to the  $1s \rightarrow t_{2g}$  transition) and a weak peak (ii: 7716.0 eV, assigned to the  $1s \rightarrow e_g$  transition), indicative of a non-centrosymmetric tetrahedral (Td) arrangement of the Co ions in POM2.<sup>[68]</sup> Furthermore, POM2 displays a visible rising edge peak (iii: 7722.5 eV,  $1s \rightarrow 4p$ ) with an edge energy of 7720.5 eV. These geometry assignments are consistent with the previously reported XANES of relevant Co-complexes (e.g.,  $\text{Na}_{10}[\text{Co}_4(\text{H}_2\text{O})_2(\text{VW}_9\text{O}_{34})_2] \cdot 35\text{H}_2\text{O}$ ,  $\text{K}_5[\text{CoW}_{12}\text{O}_{40}] \cdot 20\text{H}_2\text{O}$ ).<sup>70-72</sup>

The Co K edge spectrum of MMO (Figure 1c) is free of the strong pre-edge features existing in POM2, while it shows considerably matching edge energy (7719 eV) and white line peak energy to those of POM1, indicative of  $\text{Co}^{2+}$  oxidation state and Oh geometry of Co element in the MMO. According to Figure 1d, the ex-situ XANES W L3 edge spectra of MMO shows an edge energy of 10204.6 eV, which is nearly identical to that of  $\text{W}^{6+}$  containing references POM1, POM2 and  $\text{WO}_3$  and

significantly different from  $W^{4+}$  reference  $WO_2$ . In addition, the broad white line feature shown in POM1, POM2 and  $WO_3$ ,<sup>73,74</sup> was also observed in MMO, demonstrating the Oh coordination geometry of W element with  $W^{6+}$  oxidation state. The ex-situ XANES Cu K edge spectrum of MMO shows a sharp edge peak ( $1s \rightarrow 4p$ ) at 8981.4 eV (labeled as i, inset Figure 1e) and the absence of the pre-edge peak features existing in the  $Cu^{2+}$

reference ( $CuO$ , 8979 eV,  $1s \rightarrow 3d$ ).<sup>75</sup> Additionally, the MMO shows an edge energy of 8985 eV, which is between that of  $Cu^+$  (8984 eV) and  $Cu^{2+}$  (8986 eV),<sup>76,77</sup> suggesting the presence of a mixture of  $Cu^+$  and  $Cu^{2+}$  in the MMO. This is further confirmed by the linear combination analysis, giving a ratio of 4:1 ( $Cu^+ : Cu^{2+}$ , Figure 1f, Table S1).<sup>78</sup>

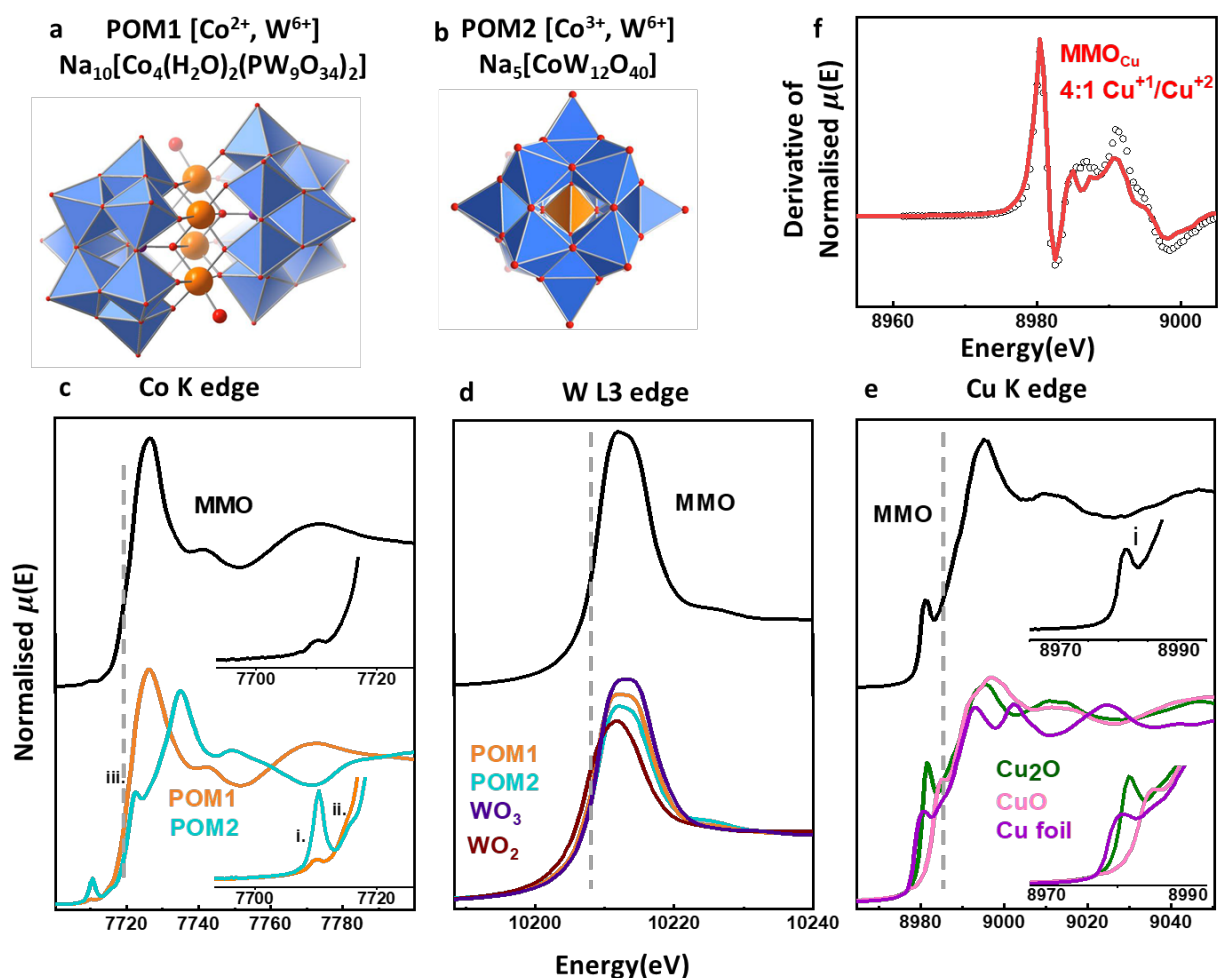


Figure 1. (a) and (b) Structures of POM1 and POM2, color scheme: Co atoms in orange, O in red and W in blue. Ex-situ XANES spectra of (c) Co K edge, (d) W L3 edge, (e) Cu K edge of MMO and references. (f) Linear combination analysis of the MMO at Cu K edge.

Next, the experimental ex-situ EXAFS data obtained for POM1 and POM2 at the Co K and W L edges were simulated based on their structures obtained previously via single-crystal X-ray diffraction.<sup>70-72</sup> The simulated structure gave good-to-excellent reproduction of the experimental results (R- and K-space fitting of POM1 and POM2 data are shown in Figures S2-S3, Table S2). The dominant interaction in both POM1 and POM2 is metal-oxygen scattering with average bond lengths of 2.019 ( $n=2$ ), 2.086 ( $n=2$ ), 2.258 Å ( $n=2$ ) in POM1 and 1.805 Å ( $n=4$ ) in POM 2 ( $n$ : the number of scattering paths), which significantly surpassed the metal-metal scattering. This highlights the critical role of the metal-oxygen coordination environment in shaping the overall structural characteristics of both model POMs. Furthermore, an in-depth analysis of second shell fitting of POM1 revealed intense Co-Co scattering at 3.2 Å and weak Co-W scattering at 3.5 Å, indicating the presence of neighboring Co and W atoms. In contrast, a pronounced Co-W scattering

at ca. 3.5 Å was observed in POM2, consistent with the exclusive Co-W coordination.

Following the structural studies of model POMs, we investigated the ex-situ Co K edge, Cu K edge, and W L3 edge EXAFS spectra of the MMO (Figure 3 and Table 1). The first shell of the Co K edge EXAFS data for MMO was successfully fit using an octahedral  $CoO_6$  geometry with a Co-O bond length of 2.07 Å. In addition, the second coordination shell revealed two distinct scattering paths, Co-X at distances of 2.89 Å ( $n=2$ ) and 3.06 Å ( $n=6$ ). The identity of X could not be accurately determined, and either Co or Cu centers gave equally good fit to the experimental data, due to similar atomic numbers (Figure S4 and Table S3). Notably, no Co-W scattering was observed in the Co K-edge EXAFS, which is either due to a small number of neighboring W-atoms (similar to the EXAFS of POM 1, Figure 2a), or a completely W-free environment.<sup>70-72</sup>

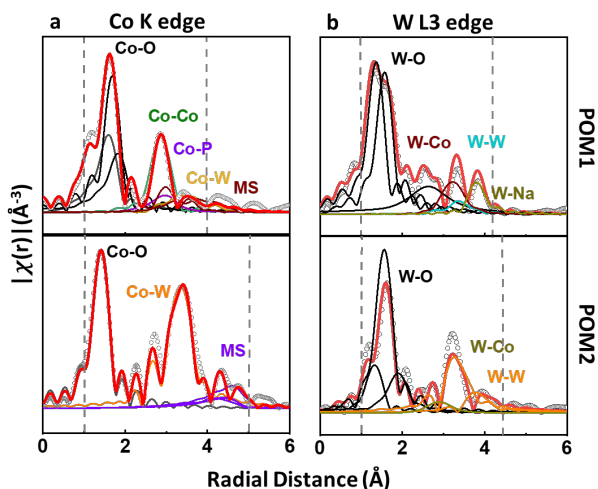


Figure 2. Ex-situ EXAFS of POM references. (a) Co K edge of POM1 (top) and POM2 (bottom), (b) W L3 edge of POM1 (top) and POM2 (bottom), where the experimental data is in circles and fitted data is the red solid line. Individual path lengths are shown with solid lines. MS: multiple atoms scattering paths.

The Cu K-edge EXAFS data were fit using a 1:4 combination of two types of Cu environments, in agreement with the presence of Cu(II) (20%) and Cu(I) (80%) ions revealed in the XANES Cu K-edge results. The first shell of Cu(I) species was modeled as tetrahedral CuO, while the Cu(II) species were modeled as square-planar Cu<sub>2</sub>O, and the Cu-O bond lengths obtained from the fit were 1.85 Å (n = 3) and 1.96 Å (n = 1), respectively.<sup>79,80</sup> Additionally, the secondary coordination sphere fitting revealed two distinctive Cu-X peaks with bond lengths of 3.00 Å (n = 6) and 3.12 Å (n = 3) (here, X=Co or Cu, Figure S5 and Table S4, SI).

The EXAFS analysis at the W L3 edge was performed using an octahedral WO<sub>6</sub> first shell with two bond lengths at 1.88 Å (n = 3) and 3.01 Å (n = 3, Figure 3c). This observation implies the existence of either two distinct WO<sub>6</sub> Oh environments in a 1:1 ratio or one distorted trigonal prismatic configuration. The trigonal prismatic configuration of WO<sub>6</sub> is rare, but it has been observed in mixed metal oxides with AABB packing arrangement of metal-oxo clusters.<sup>81</sup> Moreover, the presence of another metal (possibly Co or Cu) was detected at a distance of 3.37 Å (n=2). Notably, no W-W scattering paths were observed, suggesting that all W atoms in the MMO are isolated and surrounded by Co or Cu metal oxides (Figure S6 and Table S5). These extensive ex-situ characterizations lay a solid foundation for subsequent in-situ XAS studies, which will contribute to an in-depth understanding of the dynamic structural evolution of MMO as well as the potential catalytic mechanism.

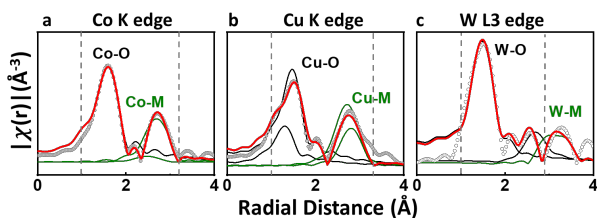


Figure 3. EXAFS data fitting of (a) Co K edge, (b) Cu K edge, and (c) W L3 edge of MMO where the experimental data is in circles and fitted data is the red solid line. Solid grey dash lines show

the data window that have been fitted. Metal-oxygen scattering is shown in black and metal-metal scattering is shown in green.

Table 1. Summary of structure information of MMO.

	Co K edge	Cu K edge	W L3 edge
Oxidation state	Co <sup>2+</sup>	Cu <sup>+</sup> /Cu <sup>2+</sup>	W <sup>6+</sup>
Geometry	Oh	Td / SP	Oh
Fitted bond lengths (X = Cu, Co)	Co-O:	Cu-O:	W-O:
	2.07 Å	1.85 Å, 1.96 Å	1.88 Å, 3.01 Å
	Co-X:	Cu-X:	W-X:
	2.89 Å, 3.06 Å	3.00 Å, 3.13 Å	3.37 Å

**XAS-EC:** Prior to the in-situ XAS studies, the electrocatalytic performance of the solid-state MMO (drop-casted on carbon paper, MMO@CP) was examined for both HER and OER in alkaline electrolyte (0.1 M KOH, pH 12.8). Linear sweep voltammetry (LSV) polarization curves (Figure 4a, c) show that the MMO@CP exhibits the satisfying activity with overpotentials of 365 mV and 447 mV for HER and OER at the current density of 10 mA/cm<sup>2</sup> (based on geometric surface area). The overpotential is somewhat higher than the previously reported composite electrode,<sup>27</sup> which we attribute to the loss of the electrode/catalyst bonding interaction during the transfer of the MMO sample from the Cu foam growth substrate to the carbon electrode. To assess the long-term stability of the MMO@CP, chronoamperometry was conducted over 5 h. The current density was stable under both HER and OER conditions and the comparison of LSV curves before and after 5 h of electrolysis (Insets in Figure 4b, d) displayed nearly identical performance. The current density for HER exhibited an initial increase in the current density, hinting at the possible electrochemical generation of the catalytically active species (Figure 4b). The OER activity remained at 82% activity after the 5 h period (Figure 4d), demonstrating the extraordinary stability of solid-state MMO under harsh oxidative electrocatalytic conditions.<sup>27</sup>

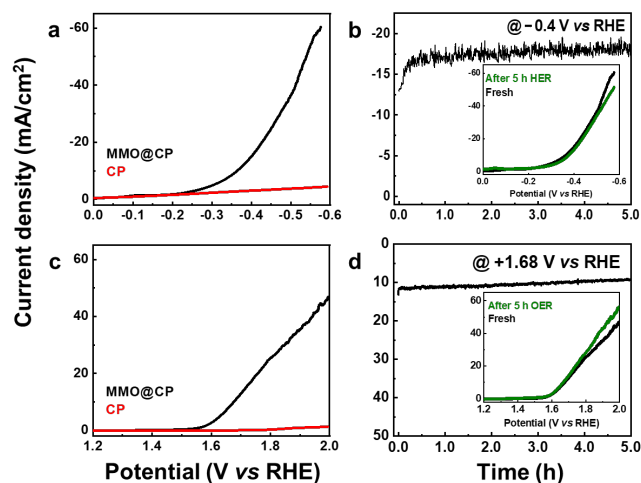


Figure 4. Catalytic performance of MMO@CP for HER and OER. LSV polarization curves of MMO@CP and CP reference for HER (a) and OER (c), scan rate: 5 mV/s; chronoamperometric studies



of (c) HER (-0.4 V vs RHE) and (d) OER (+1.68 V vs RHE); inset: LSV comparison of HER and OER performance.

To gain critical insights into the structural evolution of the MMO under operating conditions, the XAS-EC measurements were conducted at open circuit potential (OCP) and electrocatalytic potentials (+1.68 V vs RHE for OER and -0.4 V for HER) using a custom-built spectroelectrochemical cell (Figure S7, SI). The Co K edge XANES spectra observed under OER condition (Figure 5a) show a noticeable positive shift of the edge energy (from 7719 eV to 7722 eV), indicative of the oxidation of  $\text{Co}^{2+}$  to  $\text{Co}^{3+}$ . This transformation is further supported by the oxidation states analysis (Figure S8, SI). Additionally, the increase in the intensity of the pre-edge peak (7711 eV,  $s \rightarrow d$ , Figure 5a inset) is expected for the increase in the 3d vacancy that takes place when the cobalt ion is oxidized. The increased pre-edge intensity may also be a reporter of a deviation from the centrosymmetric Oh geometry. Such loss in symmetry is known to lead to increased 3d-4p hybridization of the metal orbitals, thus increasing the “allowedness” of the  $1s \rightarrow 3d$  transition.<sup>82,83</sup> In contrast, under HER condition, no edge energy changes were observed, indicative of the maintained pristine  $\text{Co}^{2+}$  in the MMO. The increased pre-edge peak intensity and the expansion of the white line region demonstrates a change in the coordination environment around the Co site during both OER and HER.

The Cu K edge XANES spectra (Figure 5b) exhibit no significant alterations in pre-edge and edge energy (from 8985 eV to 8984.9 eV) during OER, implying oxidation-state-stable property of the Cu sites during OER. In contrast, Cu edge energy was observed to shift to a lower value (from 8985 eV to 8984.5 eV, Figure S9, SI) with the successive scans during HER, implying reduction of  $\text{Cu}^+/\text{Cu}^{2+}$  ions to metallic Cu NPs. Linear combination analysis of these scans also indicated the formation of metallic Cu (from 0 to 62.9%), while the  $\text{Cu}^+$  was found to be diminished (from 80% to 21.6%) and  $\text{Cu}^{2+}$  (from 20% to 15.5%) (Table S6, Figure S10, SI). This dynamic transformation suggested that the Cu(I) sites are the pre-catalytic species that are electrochemically reduced to the catalytically active Cu NPs.

The W L3 edge XANES spectra displayed no discernible changes in either OER or HER (Figure 5c). The stability of the W sites implied that it may act as a passive spectator, providing structural support to the active Co and Cu sites responsible for OER and HER, respectively. Furthermore, the absence of significant changes in the W coordination environment was observed by the retained broad white line features, indicating that the W atoms remained isolated and surrounded by Co or Cu metal oxides. For a summary of the structural changes of Co, Cu and W in the MMO, see Table S7.

Next, XAS-EC EXAFS measurements were performed to capture the local structural evolution of the MMO during electrocatalytic water splitting. The analysis of the Co K-edge EXAFS during OER imply the retention of the octahedral geometry and the shortening of the Co-O bond length from 2.07 Å to 1.9 Å, along with the visible decrease in distances of one of the Co-X pathways (from 3.06 Å to 2.9 Å, Figure 6a). Under HER condition, the Oh coordination of Co underwent a distortion characterized by a pronounced elongation of the two axial Co-O bonds (from 2.07 Å to 2.27 Å), while the length of the four equatorial Co-O bonds remains unchanged. Simultaneously, there was an increase in the Co-X bond length from 2.89 Å to 3.56 Å ( $n = 2$ ), and 3.06 Å ( $n = 6$ ) to 3.25 Å ( $n = 4$ ) (Table S8, Figure S11).<sup>84</sup>

The analysis of the Cu K edge EXAFS spectra during OER shows that the both Cu moieties remained the original coordination environment, with Cu-O bond lengths increasing to 1.93 Å from 1.85 Å ( $n = 3$ ,  $\text{Cu}^+$ ), and 2.16 Å from 1.96 Å ( $n = 1$ ,  $\text{Cu}^{2+}$ , Figure 6b). Furthermore, the bond length for Cu-X decreased to 2.59 Å ( $n = 6$ ) from 3.0 Å ( $n = 6$ ), and 2.26 Å ( $n = 2$ ) from 3.12 Å ( $n = 3$ , Table S9 and Figure S12). More drastic EXAFS changes were observed during HER, where Cu species underwent a compositional transformation to metallic copper NPs, observed as the growth of the new Cu-Cu scattering feature at 2.7 Å (Figure 6b). This feature grows with electrolysis time from CN = 0 to 7 over the period of 4 scans. The size of the in-situ formed Cu NPs was evaluated from the number of Cu-Cu scattering paths, using the calibration curve obtained for Cu-Cu scattering in nanoparticles with known diameters, reported in the previous studies.<sup>85-87</sup> We find that the Cu-NP diameter increases over the time of XAS-EC scans, reaching approximately 9 nm at the end of 4<sup>th</sup> scan (Table S10 and Figure S13).

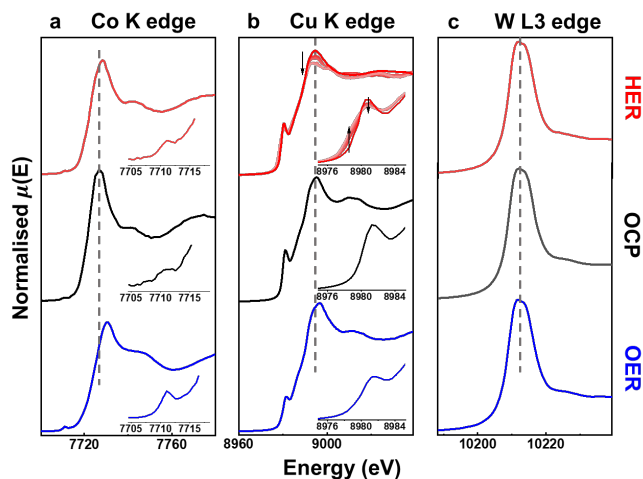


Figure 5. In-situ XAS-EC XANES spectra of (a) Co K edge, (b) Cu K edge, (c) W L3 edge of MMO under -0.4 V vs RHE (for HER), 0 V vs RHE (for OCP) and +1.68 V vs RHE (for OER). The insets show the pre-edge region of corresponding curves.

Based on the W L3 edge EXAFS spectra (Figure 6c), the Oh coordination environment around W became more distorted during both OER and HER. OER was accompanied by the decrease in one W-O bond length from 3.01 Å ( $n=3$ ) to 2.46 Å ( $n=1$ ) and 2.83 Å ( $n=2$ ), while the other remained constant under error bar (1.88 Å ( $n=3$ )). In contrast, the length of one W-O bond was reduced from 3.01 Å ( $n=3$ ) to 2.35 Å ( $n=1$ ) under HER conditions, while the other W-O bond lengths (1.88 Å ( $n=3$ ) and 3.01 Å ( $n=2$ )) remained unchanged (Table S11 and Figure S14). No significant changes in W-X bond lengths were observed.<sup>84</sup>

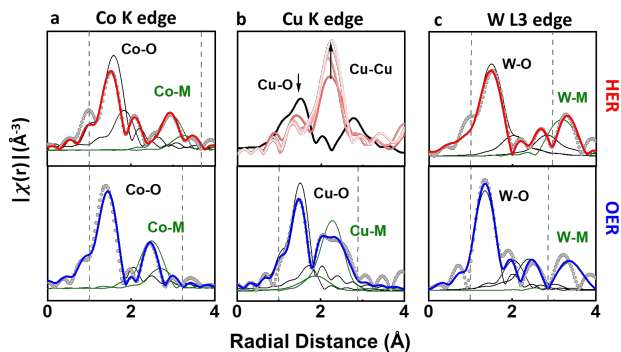


Figure 6. XAS-EC EXAFS measurement of (a) Co K edge, (b) Cu K edge, (c) W L3 edge of MMO@CP under -0.4 V vs RHE (for HER in red), 0 V vs RHE (for OCP in black), and +1.68 V vs RHE (for OER in blue). Grey line: M-O scattering, green line: M-M scattering, vertical dash line:  $r$  region of  $R$  space used for fitting, grey circles: experimental data.

**Mechanisms:** The insights into HER and OER mechanisms were obtained by combining electrochemical Tafel slope analysis and XAS-EC data fitting. For HER, Tafel slopes exceeding 120 mV/decade (theoretical limit for Tafel slope analysis for HER), were obtained for the MMO@CP (142-208 mV/decade, Figure S15a), while even higher Tafel slopes were observed in the previous study on the composite MMO@Cu electrode (335 mV/decade).<sup>27</sup> Notably, such high Tafel slopes have been reported for HER in basic media, where the water dissociation step ( $\text{H}_2\text{O} \rightarrow \text{H}^+ + \text{OH}^-$ ) was proposed as the rate-determining step (RDS).<sup>88-90</sup> As aforementioned, the XAS-EC data of the MMO displayed notable changes in the Cu center during HER, indicating the formation of Cu NPs (Table S6). Based on these findings, we propose a mechanism that involves the electrochemical conversion of Cu(I)-oxo pre-catalyst to catalytically active Cu NPs, whose protonation to form surface M-H species is the RDS (Figure 7). The subsequent  $\text{H}_2$  releasing step may occur either via Heyrovsky or Tafel pathway. The established reactivity of Cu-np in the literature further supports this observation.<sup>91-93</sup> It is likely that the nanostructured Cu sites exhibit improved HER kinetics via exposing more active sites on the metal surface.<sup>94</sup>

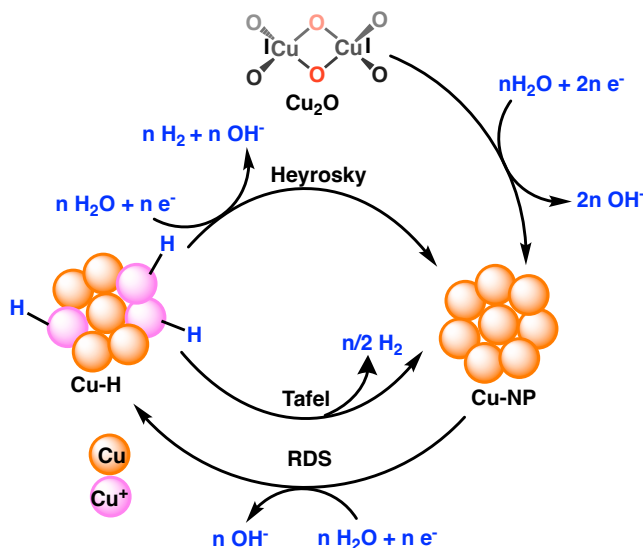
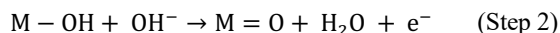
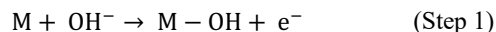
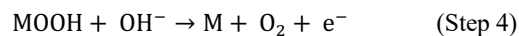


Figure 7. Proposed mechanism for HER.

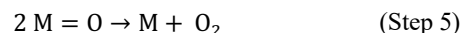
For OER, the Tafel slopes were derived for two possible OER mechanisms: the single-site (SS) and the double-site (DS) models. Both mechanisms involve the formation of M-OH and M=O intermediates on the MMO surface, where M denotes an active site on the surface of the MMO catalyst:



The SS model proceeds via the formation of MOOH intermediate:



While the DS model proceeds via the bimetallic O-O coupling:



The derivation of Tafel slopes assuming different rate-determining steps is shown in SI (Section S4.1.), while the calculated Tafel slopes are shown in Figure 8a. Different RDSs can be distinguished at low overpotentials, where 120 mV/decade slope is expected when Step 1 is RDS. The Tafel slopes of 40, 23.6, 16 or 14 mV/decade are expected when Step 2, Step 3, Step 4 or Step 5 is RDS. Experimental Tafel slopes of the MMO were derived from LSV data (Figure 8b, Figure S15b), illustrating values increasing from 16 mV/decade at 0.07 V overpotential to 180 mV/decade at 0.25 V overpotential. Given that the experimental slope drops below 20 mV/decade at low overpotentials (below 0.071 V), we hypothesize that the RDS is the removal of  $\text{O}_2$ , either via Step 4 (for the SS mechanism, with a Tafel slope of 16 mV/decade) or via Step 5 (for the DS mechanism with a Tafel slope of 14 mV/decade). In this context, the OER bottleneck intermediates are identified to be either MOOH (for SS mechanism) or M=O (for DS mechanism).

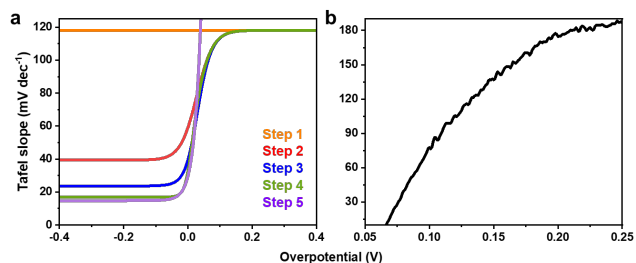


Figure 8. (a) Simulated and (b) experimental Tafel slope analysis for OER.

According to the XAS-EC data, Co and Cu centers demonstrated chemical and structural evolution during OER (Figures 5 and 6). Notably, only the Co center underwent a change in the oxidation state from  $\text{Co}^{2+}$  to  $\text{Co}^{3+}$ , while the Cu centers maintain their original  $\text{Cu}^{+2+}$  states. Based on these observations, a SS mechanism was proposed involving  $\text{Co}^{\text{III}}\text{-OOH}$  as the bottleneck intermediate before the RDS of  $\text{O}_2$  evolution. As depicted in Figure 9, the catalytic cycle includes cooperative catalysis by a redox-active Co center  $\text{Co}^{\text{II}}\text{-H}_2\text{O}$  and redox-innocent Cu. This proposed mechanism is supported by the XAS-EC data, which show the elongation of the Cu-O and the compression of Co-O

bond lengths in the intermediate  $\text{Co}^{\text{III}}\text{-OOH}$ , a structural change that is consistent with the increased charge of the  $\text{Co}^{3+}$  center. This change in the Co-O-Cu bond lengths indicates the mechanism by which the neighboring Cu-atoms tune the reactivity of the  $\text{Co}^{\text{III}}\text{-OOH}$  intermediate, facilitating the evolution of  $\text{O}_2$ . Previous studies involving mixed-metal Co/Cu oxides and sulfides have also reported a synergy between the two metals during OER.<sup>95,96</sup> In general, the synergy was attributed to the modulation of reactive, high-spin octahedral Co(III) intermediates and these conclusions are in agreement with our experimental observations. Our observation of bond length changes in the Co-O-Cu moiety may be a structural change critical for the formation of either more reactive or more stabilized Co(III)-hydroperoxides and may be explored as a criterium for the design of future MMO catalysts.

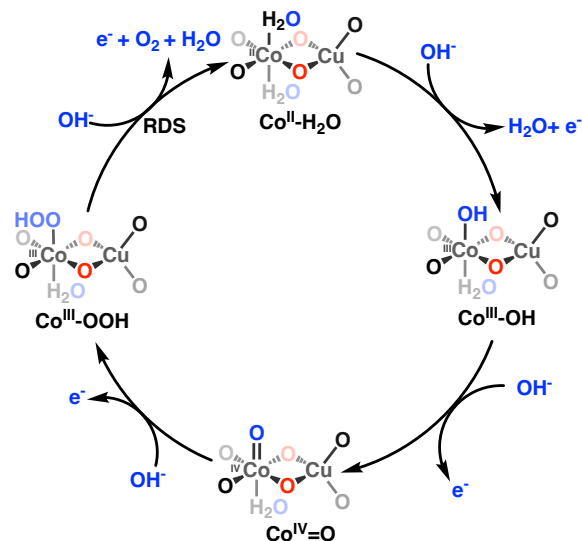


Figure 9. Proposed mechanism of the SS model for OER.

## CONCLUSION:

In summary, by employing synchrotron-based XAS, combined with the Tafel analysis, we reveal the complex catalytic behavior exhibited by the Co-Cu-W MMO@CP under alkaline OER and HER. The HER was found to proceed via catalytic Cu NPs, electro-generated from the Cu(I)-oxo pre-catalysts. We also find that the Cu NPs undergo dynamic evolution during catalysis, with the NP diameter increasing during the first few hours of electrolysis. The OER was found to proceed via  $\text{Co}^{\text{III}}\text{-OOH}$  bottleneck intermediate, whose electronic behavior and structure is tuned by the neighboring Cu atoms. The identification of key redox-active centers, determination of RDS, and revelation of intermediates, signifies a substantial leap in our understanding of the fundamental mechanisms of electrocatalytic water splitting driven by the Co-Cu-W MMO. This not only guides the knowledge-based design of efficient MMO electrocatalysts, but also underscore the significance of synergistic interactions within MMO systems, thereby laying a solid foundation for the design of next-generation electrocatalysts for challenging energy conversion and storage reactions.

## ASSOCIATED CONTENT

### Supporting Information

Contains materials synthesis and its characterization, experimental details for XAS measurements, Tafel slope derivation for different OER steps.

## AUTHOR INFORMATION

### Corresponding Author

**Ksenija D. Glusac** - Department of Chemistry, University of Illinois Chicago, Chicago, Illinois 60607, United States; Chemical Sciences and Engineering, Argonne National Laboratory, Lemont, Illinois 60439, United States; orcid.org/0000-0002-2734-057X; Email: [glusac@uic.edu](mailto:glusac@uic.edu)

**Dandan Gao** - Department of Chemistry, Johannes Gutenberg University Mainz, Mainz 55128, Germany; Email: [dandan.gao@uni-mainz.de](mailto:dandan.gao@uni-mainz.de).

### Author Contributions

The manuscript was written through contributions of all authors. / All authors have given approval to the final version of the manuscript.

### Notes

The authors declare no conflict of interest.

## ACKNOWLEDGMENT

This work is supported by the National Science Foundation (CAS 2102247). We also acknowledge support from the Advanced Photon Source, a U.S. Department of Energy (DOE) Office of Science User Facility at Argonne National Laboratory, supported by the U.S. DOE Office of Science-Basic Energy Sciences, under Contract No. DE-AC02-06CH11357. This work was also financially supported by Walter Benjamin Fellowship (project no. 510966757) and the Top Level Research Area SusInnoScience of the federal state of Rheinland-Pfalz.

## ABBREVIATIONS

XAS, X-ray Absorption Spectroscopy; XANES, X-ray Absorption Near-Edge structure; EXAFS, extended X-ray Absorption Fine Structure; XAS-EC, X-ray Absorption Spectroscopy coupled with Electrochemistry; RDS, Rate Determining Step; MMO, Mixed Metal Oxide; Oh, Octahedral; Td, Tetrahedral; SP, Square Planar; Cu-NP, Copper Nanoparticle.

## REFERENCES

- (1) Ifkovits, Z. P.; Evans, J. M.; Meier, M. C.; Papadantonakis, K. M.; Lewis, N. S. Decoupled Electrochemical Water-Splitting Systems: A Review and Perspective. *Energy and Environmental Science*. Royal Society of Chemistry September 1, 2021, pp 4740–4759. <https://doi.org/10.1039/d1ee01226f>.
- (2) Lamers, P.; Ghosh, T.; Upasani, S.; Sacchi, R.; Daioglou, V. Linking Life Cycle and Integrated Assessment Modeling to Evaluate Technologies in an Evolving System Context: A Power-to-Hydrogen Case Study for the United States. *Environ Sci Technol* **2023**, *57* (6), 2464–2473. <https://doi.org/10.1021/acs.est.2c04246>.
- (3) Geletii, Y. V.; Huang, Z.; Hou, Y.; Musaev, D. G.; Lian, T.; Hill, C. L. Homogeneous Light-Driven Water Oxidation Catalyzed by a Tetraruthenium Complex with All Inorganic Ligands. *J Am Chem Soc* **2009**, *131* (22), 7522–7523. <https://doi.org/10.1021/ja901373m>.
- (4) Yu, M.; Budiyanto, E.; Tüysüz, H. Principles of Water Electrolysis and Recent Progress in Cobalt-, Nickel-, and Iron-Based Oxides for the Oxygen Evolution Reaction. *Angewandte Chemie - International Edition*.

John Wiley and Sons Inc January 3, 2022.  
<https://doi.org/10.1002/anie.202103824>.

(5) Wang, M.; Wa, Q.; Bai, X.; He, Z.; Samarakoon, W. S.; Ma, Q.; Du, Y.; Chen, Y.; Zhou, H.; Liu, Y.; Wang, X.; Feng, Z. The Restructuring-Induced CoOx Catalyst for Electrochemical Water Splitting. *J Am Chem Soc* **2021**, *1* (12), 2216–2223. <https://doi.org/10.1021/jacsau.1c00346>.

(6) Huynh, M.; Bediako, D. K.; Nocera, D. G. A Functionally Stable Manganese Oxide Oxygen Evolution Catalyst in Acid. *J Am Chem Soc* **2014**, *136* (16), 6002–6010. <https://doi.org/10.1021/ja413147e>.

(7) Xu, L.; Jiang, Q.; Xiao, Z.; Li, X.; Huo, J.; Wang, S.; Dai, L. Plasma-Engraved Co<sub>3</sub>O<sub>4</sub> Nanosheets with Oxygen Vacancies and High Surface Area for the Oxygen Evolution Reaction. *Angewandte Chemie* **2016**, *128* (17), 5363–5367. <https://doi.org/10.1002/ange.201600687>.

(8) Luo, W.; Hu, J.; Diao, H.; Schwarz, B.; Streb, C.; Song, Y.-F. Stabile Polyoxometallat-Nickelschaum-Elektroden Für Elektrochemische Sauerstoffentwicklung Im Alkalischen Milieu. *Angewandte Chemie* **2017**, *129* (18), 5023–5026. <https://doi.org/10.1002/ange.201612232>.

(9) Zhang, R.; Pan, L.; Guo, B.; Huang, Z. F.; Chen, Z.; Wang, L.; Zhang, X.; Guo, Z.; Xu, W.; Loh, K. P.; Zou, J. J. Tracking the Role of Defect Types in Co<sub>3</sub>O<sub>4</sub> Structural Evolution and Active Motifs during Oxygen Evolution Reaction. *J Am Chem Soc* **2022**. <https://doi.org/10.1021/jacs.2c10515>.

(10) Lu, X. F.; Gu, L. F.; Wang, J. W.; Wu, J. X.; Liao, P. Q.; Li, G. R. Bimetal-Organic Framework Derived CoFe<sub>2</sub>O<sub>4</sub>/C Porous Hybrid Nanorod Arrays as High-Performance Electrocatalysts for Oxygen Evolution Reaction. *Advanced Materials* **2017**, *29* (3). <https://doi.org/10.1002/adma.201604437>.

(11) Li, N.; Bediako, D. K.; Hadt, R. G.; Hayes, D.; Kempa, T. J.; Von Cube, F.; Bell, D. C.; Chen, L. X.; Nocera, D. G. Influence of Iron Doping on Tetravalent Nickel Content in Catalytic Oxygen Evolving Films. *Proc Natl Acad Sci U S A* **2017**, *114* (7), 1486–1491. <https://doi.org/10.1073/pnas.1620787114>.

(12) Ling, T.; Zhang, T.; Ge, B.; Han, L.; Zheng, L.; Lin, F.; Xu, Z.; Hu, W. Bin; Du, X. W.; Davey, K.; Qiao, S. Z. Well-Dispersed Nickel- and Zinc-Tailored Electronic Structure of a Transition Metal Oxide for Highly Active Alkaline Hydrogen Evolution Reaction. *Advanced Materials* **2019**, *31* (16). <https://doi.org/10.1002/adma.201807771>.

(13) Gong, R.; Gao, D.; Liu, R.; Sorsche, D.; Biskupek, J.; Kaiser, U.; Rau, S.; Streb, C. Self-Activation of a Polyoxometalate-Derived Composite Electrocatalyst for the Oxygen Evolution Reaction. *ACS Appl Energy Mater* **2021**, *4* (11), 12671–12676. <https://doi.org/10.1021/acsaem.1c02399>.

(14) Ling, T.; Zhang, T.; Ge, B.; Han, L.; Zheng, L.; Lin, F.; Xu, Z.; Hu, W. Bin; Du, X. W.; Davey, K.; Qiao, S. Z. Well-Dispersed Nickel- and Zinc-Tailored Electronic Structure of a Transition Metal Oxide for Highly Active Alkaline Hydrogen Evolution Reaction. *Advanced Materials* **2019**, *31* (16). <https://doi.org/10.1002/adma.201807771>.

(15) Naito, T.; Shinagawa, T.; Nishimoto, T.; Takane, K. Recent Advances in Understanding Oxygen Evolution Reaction Mechanisms over Iridium Oxide. *Inorganic Chemistry Frontiers*. Royal Society of Chemistry

June 7, 2021, pp 2900–2917. <https://doi.org/10.1039/d0qi01465f>.

(16) Gao, J.; Liu, Y.; Liu, B.; Huang, K. W. Progress of Heterogeneous Iridium-Based Water Oxidation Catalysts. *ACS Nano*. American Chemical Society November 22, 2022, pp 17761–17777. <https://doi.org/10.1021/acsnano.2c08519>.

(17) Reier, T.; Nong, H. N.; Teschner, D.; Schlögl, R.; Strasser, P. Electrocatalytic Oxygen Evolution Reaction in Acidic Environments – Reaction Mechanisms and Catalysts. *Advanced Energy Materials*. Wiley-VCH Verlag January 11, 2017. <https://doi.org/10.1002/aenm.201601275>.

(18) Zhao, Y.; Hernandez-Pagan, E. A.; Vargas-Barbosa, N. M.; Dysart, J. L.; Mallouk, T. E. A High Yield Synthesis of Ligand-Free Iridium Oxide Nanoparticles with High Electrocatalytic Activity. *Journal of Physical Chemistry Letters* **2011**, *2* (5), 402–406. <https://doi.org/10.1021/jz200051c>.

(19) Moschkowitsch, W.; Zion, N.; Honig, H. C.; Levy, N.; Cullen, D. A.; Elbaz, L. Mixed-Metal Nickel-Iron Oxide Aerogels for Oxygen Evolution Reaction. *ACS Catal* **2022**, *12* (19), 12162–12169. <https://doi.org/10.1021/acscatal.2c03351>.

(20) Ahmed, J.; Alhokbany, N.; Ahamad, T.; Alshehri, S. M. Investigation of Enhanced Electro-Catalytic HER/OER Performances of Copper Tungsten Oxide@reduced Graphene Oxide Nanocomposites in Alkaline and Acidic Media. *New Journal of Chemistry* **2022**, *46* (3), 1267–1272. <https://doi.org/10.1039/d1nj04617a>.

(21) Xiong, B.; Chen, L.; Shi, J. Anion-Containing Noble-Metal-Free Bifunctional Electrocatalysts for Overall Water Splitting. *ACS Catal* **2018**, *8* (4), 3688–3707. <https://doi.org/10.1021/acscatal.7b04286>.

(22) Hou, J.; Sun, Y.; Wu, Y.; Cao, S.; Sun, L. Promoting Active Sites in Core-Shell Nanowire Array as Mott-Schottky Electrocatalysts for Efficient and Stable Overall Water Splitting. *Adv Funct Mater* **2018**, *28* (4). <https://doi.org/10.1002/adfm.201704447>.

(23) Kuang, M.; Han, P.; Wang, Q.; Li, J.; Zheng, G. CuCo Hybrid Oxides as Bifunctional Electrocatalyst for Efficient Water Splitting. *Adv Funct Mater* **2016**, *26* (46), 8555–8561. <https://doi.org/10.1002/adfm.201604804>.

(24) Jin, Y.; Wang, H.; Li, J.; Yue, X.; Han, Y.; Shen, P. K.; Cui, Y. Porous MoO<sub>2</sub> Nanosheets as Non-Noble Bifunctional Electrocatalysts for Overall Water Splitting. *Advanced Materials* **2016**, *28* (19), 3785–3790. <https://doi.org/10.1002/adma.201506314>.

(25) Yu, L.; Zhou, H.; Sun, J.; Qin, F.; Yu, F.; Bao, J.; Yu, Y.; Chen, S.; Ren, Z. Cu Nanowires Shelled with NiFe Layered Double Hydroxide Nanosheets as Bifunctional Electrocatalysts for Overall Water Splitting. *Energy Environ Sci* **2017**, *10* (8), 1820–1827. <https://doi.org/10.1039/c7ee01571b>.

(26) Yan, X.; Tian, L.; Li, K.; Atkins, S.; Zhao, H.; Murowchick, J.; Liu, L.; Chen, X. FeNi<sub>3</sub>/NiFeOx Nanohybrids as Highly Efficient Bifunctional Electrocatalysts for Overall Water Splitting. *Adv Mater Interfaces* **2016**, *3* (22). <https://doi.org/10.1002/admi.201600368>.

(27) Gao, D.; Liu, R.; Biskupek, J.; Kaiser, U.; Song, Y.; Streb, C. Modular Design of Noble-Metal-Free Mixed Metal Oxide Electrocatalysts for Complete Water Splitting. *Angewandte Chemie* **2019**, *131* (14), 4692–4696. <https://doi.org/10.1002/ange.201900428>.

(28) She, Z. W.; Kibsgaard, J.; Dickens, C. F.; Chorkendorff, I.; Nørskov, J. K.; Jaramillo, T. F.



Combining Theory and Experiment in Electrocatalysis: Insights into Materials Design. *Science*. American Association for the Advancement of Science January 13, 2017. <https://doi.org/10.1126/science.aad4998>.

(29) Wang, H.; Zhang, K. H. L.; Hofmann, J. P.; de la Peña O'Shea, V. A.; Oropoza, F. E. The Electronic Structure of Transition Metal Oxides for Oxygen Evolution Reaction. *Journal of Materials Chemistry A*. Royal Society of Chemistry September 21, 2021, pp 19465–19488. <https://doi.org/10.1039/d1ta03732c>.

(30) Xie, X.; Du, L.; Yan, L.; Park, S.; Qiu, Y.; Sokolowski, J.; Wang, W.; Shao, Y. Oxygen Evolution Reaction in Alkaline Environment: Material Challenges and Solutions. *Advanced Functional Materials*. John Wiley and Sons Inc May 1, 2022. <https://doi.org/10.1002/adfm.202110036>.

(31) Song, F.; Bai, L.; Moysiadou, A.; Lee, S.; Hu, C.; Liardet, L.; Hu, X. Transition Metal Oxides as Electrocatalysts for the Oxygen Evolution Reaction in Alkaline Solutions: An Application-Inspired Renaissance. *J Am Chem Soc* **2018**, *140* (25), 7748–7759. <https://doi.org/10.1021/jacs.8b04546>.

(32) Grimaud, A.; Hong, W. T.; Shao-Horn, Y.; Tarascon, J. M. Anionic Redox Processes for Electrochemical Devices. *Nature Materials*. Nature Publishing Group January 22, 2016, pp 121–126. <https://doi.org/10.1038/nmat4551>.

(33) Dau, H.; Limberg, C.; Reier, T.; Risch, M.; Roggan, S.; Strasser, P. The Mechanism of Water Oxidation: From Electrolysis via Homogeneous to Biological Catalysis. *ChemCatChem*. July 12, 2010, pp 724–761. <https://doi.org/10.1002/cctc.201000126>.

(34) Rossmeisl, J.; Qu, Z. W.; Zhu, H.; Kroes, G. J.; Nørskov, J. K. Electrolysis of Water on Oxide Surfaces. *Journal of Electroanalytical Chemistry* **2007**, *607* (1–2), 83–89. <https://doi.org/10.1016/j.jelechem.2006.11.008>.

(35) Doyle, R. L.; Lyons, M. E. G. Kinetics and Mechanistic Aspects of the Oxygen Evolution Reaction at Hydrous Iron Oxide Films in Base. *J Electrochem Soc* **2013**, *160* (2), H142–H154. <https://doi.org/10.1149/2.015303jes>.

(36) Jiao, Y.; Zheng, Y.; Jaroniec, M.; Qiao, S. Z. Design of Electrocatalysts for Oxygen- and Hydrogen-Involving Energy Conversion Reactions. *Chemical Society Reviews*. Royal Society of Chemistry April 21, 2015, pp 2060–2086. <https://doi.org/10.1039/c4cs00470a>.

(37) Benck, J. D.; Hellstern, T. R.; Kibsgaard, J.; Chakraborty, P.; Jaramillo, T. F. Catalyzing the Hydrogen Evolution Reaction (HER) with Molybdenum Sulfide Nanomaterials. *ACS Catalysis*. American Chemical Society October 8, 2014, pp 3957–3971. <https://doi.org/10.1021/cs500923c>.

(38) Rüetschi, P.; Delahay, P. Influence of Electrode Material on Oxygen Overvoltage: A Theoretical Analysis. *J Chem Phys* **1955**, *23* (3), 556–560. <https://doi.org/10.1063/1.1742029>.

(39) Subbaraman, R.; Tripkovic, D.; Chang, K. C.; Strmcnik, D.; Paulikas, A. P.; Hirunsit, P.; Chan, M.; Greeley, J.; Stamenkovic, V.; Markovic, N. M. Trends in Activity for the Water Electrolyser Reactions on 3d M(Ni,Co,Fe,Mn)Hydr(Oxy)Oxide Catalysts. *Nat Mater* **2012**, *11* (6), 550–557. <https://doi.org/10.1038/nmat3313>.

(40) Morales-Guio, C. G.; Liardet, L.; Hu, X. Oxidatively Electrodeposited Thin-Film Transition Metal (Oxy)Hydroxides as Oxygen Evolution Catalysts. *J Am Chem Soc* **2016**, *138* (28), 8946–8957. <https://doi.org/10.1021/jacs.6b05196>.

(41) Ogawa, Y.; Hideaki, I.; Takeo, F.; -, al; Liu, X.-D.; Meng, D.-D. The Electrocatalysis of Oxygen Evolution on Perovskites You May Also like Study on La<sub>2</sub>O<sub>3</sub> Wet Clean by PH Controlled Functional Water Microstructured Hydroxyl Environments and Raman Spectroscopy in Selected Basic Transition-Metal Halides.

(42) Trasatti, S. Work Function, Electronegativity, and Electrochemical Behaviour of Metals. *J Electroanal Chem Interfacial Electrochem* **1972**, *39* (1), 163–184. [https://doi.org/10.1016/S0022-0728\(72\)80485-6](https://doi.org/10.1016/S0022-0728(72)80485-6).

(43) Petrii, O. A.; Tsirlina, G. A. Electrocatalytic Activity Prediction for Hydrogen Electrode Reaction: Intuition, Art, Science. *Electrochim Acta* **1994**, *39* (11–12), 1739–1747. [https://doi.org/10.1016/0013-4686\(94\)85159-X](https://doi.org/10.1016/0013-4686(94)85159-X).

(44) Conway, B. E.; Jerkiewicz, G. Relation of Energies and Coverages of Underpotential and Overpotential Deposited H at Pt and Other Metals to the ‘Volcano Curve’ for Cathodic H<sub>2</sub> Evolution Kinetics. *Electrochim Acta* **2000**, *45* (25–26), 4075–4083. [https://doi.org/10.1016/S0013-4686\(00\)00523-5](https://doi.org/10.1016/S0013-4686(00)00523-5).

(45) Fujii, M. S.; Portegies Zwart, S. The Origin of OB Runaway Stars. *Science (1979)* **2011**, *334* (6061), 1380–1383. <https://doi.org/10.1126/science.1211927>.

(46) Huang, X.; Wang, J.; Tao, H. B.; Tian, H.; Xu, H. An Essential Descriptor for the Oxygen Evolution Reaction on Reducible Metal Oxide Surfaces. *Chem Sci* **2019**, *10* (11), 3340–3345. <https://doi.org/10.1039/C8SC04521F>.

(47) Hansen, H. A.; Man, I. C.; Studt, F.; Abild-Pedersen, F.; Bligaard, T.; Rossmeisl, J. Electrochemical Chlorine Evolution at Rutile Oxide (110) Surfaces. *Phys. Chem. Chem. Phys.* **2010**, *12* (1), 283–290. <https://doi.org/10.1039/B917459A>.

(48) Halck, N. B.; Petrykin, V.; Krtil, P.; Rossmeisl, J. Beyond the Volcano Limitations in Electrocatalysis-Oxygen Evolution Reaction. *Physical Chemistry Chemical Physics* **2014**, *16* (27), 13682–13688. <https://doi.org/10.1039/c4cp00571f>.

(49) Grimaud, A.; May, K. J.; Carlton, C. E.; Lee, Y. L.; Risch, M.; Hong, W. T.; Zhou, J.; Shao-Horn, Y. Double Perovskites as a Family of Highly Active Catalysts for Oxygen Evolution in Alkaline Solution. *Nat Commun* **2013**, *4*. <https://doi.org/10.1038/ncomms3439>.

(50) Liu, X.; Meng, J.; Zhu, J.; Huang, M.; Wen, B.; Guo, R.; Mai, L. Comprehensive Understandings into Complete Reconstruction of Precatalysts: Synthesis, Applications, and Characterizations. *Advanced Materials* **2021**, *33* (32). <https://doi.org/10.1002/adma.202007344>.

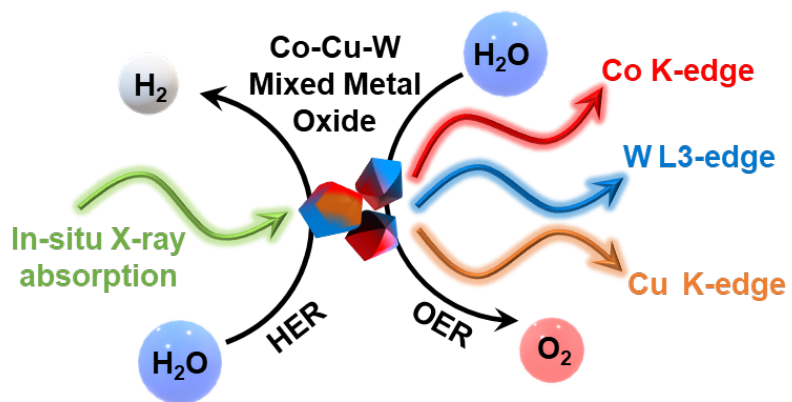
(51) Zhao, Y.; Adiyeri Saseendran, D. P.; Huang, C.; Triana, C. A.; Marks, W. R.; Chen, H.; Zhao, H.; Patzke, G. R. Oxygen Evolution/Reduction Reaction Catalysts: From *In Situ* Monitoring and Reaction Mechanisms to Rational Design. *Chem Rev* **2023**, *123* (9), 6257–6358. <https://doi.org/10.1021/acs.chemrev.2c00515>.

(52) Ahn, H. S.; Bard, A. J. Surface Interrogation Scanning Electrochemical Microscopy of Ni<sub>1-x</sub>Fe<sub>x</sub>OOH (0 <math>x</math> <math>0.27</math>) Oxygen Evolving Catalyst: Kinetics of the ‘Fast’ Iron Sites. *J Am Chem Soc* **2016**, *138* (1), 313–318. <https://doi.org/10.1021/jacs.5b10977>.

(53) Liu, D.; Shadike, Z.; Lin, R.; Qian, K.; Li, H.; Li, K.; Wang, S.; Yu, Q.; Liu, M.; Ganapathy, S.; Qin, X.; Yang, Q.; Wagemaker, M.; Kang, F.; Yang, X.; Li, B. Review of Recent Development of *In Situ/Operando* Characterization Techniques for Lithium Battery Research. *Advanced Materials* **2019**, *31* (28), 1806620. <https://doi.org/10.1002/adma.201806620>.

- (54) Ortiz Peña, N.; Ihiawakrim, D.; Han, M.; Lasalle-Kaiser, B.; Carencó, S.; Sanchez, C.; Laberty-Robert, C.; Portehault, D.; Ersen, O. Morphological and Structural Evolution of Co<sub>3</sub>O<sub>4</sub> Nanoparticles Revealed by *in Situ* Electrochemical Transmission Electron Microscopy during Electrocatalytic Water Oxidation. *ACS Nano* **2019**, *13* (10), 11372–11381. <https://doi.org/10.1021/acsnano.9b04745>.
- (55) Deng, Y.; Handoko, A. D.; Du, Y.; Xi, S.; Yeo, B. S. *In Situ* Raman Spectroscopy of Copper and Copper Oxide Surfaces during Electrochemical Oxygen Evolution Reaction: Identification of Cu<sup>III</sup> Oxides as Catalytically Active Species. *ACS Catal* **2016**, *6* (4), 2473–2481. <https://doi.org/10.1021/acscatal.6b00205>.
- (56) Handoko, A. D.; Wei, F.; Jenndy, Y.; Yeo, B. S.; Seh, Z. W. Understanding Heterogeneous Electrocatalytic Carbon Dioxide Reduction through Operando Techniques. *Nature Catalysis*. Nature Publishing Group December 1, 2018, pp 922–934. <https://doi.org/10.1038/s41929-018-0182-6>.
- (57) Tung, C.-W.; Hsu, Y.-Y.; Shen, Y.-P.; Zheng, Y.; Chan, T.-S.; Sheu, H.-S.; Cheng, Y.-C.; Chen, H. M. Reversible Adapting Layer Produces Robust Single-Crystal Electrocatalyst for Oxygen Evolution. *Nat Commun* **2015**, *6* (1), 8106. <https://doi.org/10.1038/ncomms9106>.
- (58) Zhu, Y.; Kuo, T.-R.; Li, Y.-H.; Qi, M.-Y.; Chen, G.; Wang, J.; Xu, Y.-J.; Chen, H. M. Emerging Dynamic Structure of Electrocatalysts Unveiled by *in Situ* X-Ray Diffraction/Absorption Spectroscopy. *Energy Environ Sci* **2021**, *14* (4), 1928–1958. <https://doi.org/10.1039/D0EE03903A>.
- (59) Chang, C.-J.; Zhu, Y.; Wang, J.; Chen, H.-C.; Tung, C.-W.; Chu, Y.-C.; Chen, H. M. *In Situ* X-Ray Diffraction and X-Ray Absorption Spectroscopy of Electrocatalysts for Energy Conversion Reactions. *J Mater Chem A Mater* **2020**, *8* (37), 19079–19112. <https://doi.org/10.1039/D0TA06656G>.
- (60) Stoerzinger, K. A.; Hong, W. T.; Crumlin, E. J.; Bluhm, H.; Shao-Horn, Y. Insights into Electrochemical Reactions from Ambient Pressure Photoelectron Spectroscopy. *Acc Chem Res* **2015**, *48* (11), 2976–2983. <https://doi.org/10.1021/acs.accounts.5b00275>.
- (61) Chen, J. Y. C.; Dang, L.; Liang, H.; Bi, W.; Gerken, J. B.; Jin, S.; Alp, E. E.; Stahl, S. S. Operando Analysis of NiFe and Fe Oxyhydroxide Electrocatalysts for Water Oxidation: Detection of Fe<sup>4+</sup> by Mössbauer Spectroscopy. *J Am Chem Soc* **2015**, *137* (48), 15090–15093. <https://doi.org/10.1021/jacs.5b10699>.
- (62) Kim, M.; Park, J.; Ju, H.; Kim, J. Y.; Cho, H.-S.; Kim, C.-H.; Kim, B.-H.; Lee, S. W. Understanding Synergistic Metal–Oxide Interactions of *in Situ* Exsolved Metal Nanoparticles on a Pyrochlore Oxide Support for Enhanced Water Splitting. *Energy Environ Sci* **2021**, *14* (5), 3053–3063. <https://doi.org/10.1039/D0EE02935A>.
- (63) Chen, S.; Ma, L.; Huang, Z.; Liang, G.; Zhi, C. *In Situ*/Operando Analysis of Surface Reconstruction of Transition Metal-Based Oxygen Evolution Electrocatalysts. *Cell Rep Phys Sci* **2022**, *3* (1), 100729. <https://doi.org/10.1016/j.xcrp.2021.100729>.
- (64) Shackleford, S. G. D.; Boxall, C.; Port, S. N.; Taylor, R. J. An *in Situ* Electrochemical Quartz Crystal Microbalance Study of Polycrystalline Gold Electrodes in Nitric Acid Solution. *Journal of Electroanalytical Chemistry* **2002**, *538–539*, 109–119. [https://doi.org/10.1016/S0022-0728\(02\)01218-4](https://doi.org/10.1016/S0022-0728(02)01218-4).
- (65) Risch, M.; Morales, D. M.; Villalobos, J.; Antipin, D. What X-Ray Absorption Spectroscopy Can Tell Us About the Active State of Earth-Abundant Electrocatalysts for the Oxygen Evolution Reaction\*\*. *Angewandte Chemie International Edition* **2022**, *61* (50). <https://doi.org/10.1002/anie.202211949>.
- (66) van Oversteeg, C. H. M.; Doan, H. Q.; de Groot, F. M. F.; Cuk, T. *In Situ* X-Ray Absorption Spectroscopy of Transition Metal Based Water Oxidation Catalysts. *Chem Soc Rev* **2017**, *46* (1), 102–125. <https://doi.org/10.1039/C6CS00230G>.
- (67) Wang, M.; Árnadóttir, L.; Xu, Z. J.; Feng, Z. *In Situ* X-Ray Absorption Spectroscopy Studies of Nanoscale Electrocatalysts. *Nanomicro Lett* **2019**, *11* (1), 47. <https://doi.org/10.1007/s40820-019-0277-x>.
- (68) Yang, Y.; Wang, Y.; Xiong, Y.; Huang, X.; Shen, L.; Huang, R.; Wang, H.; Pastore, J. P.; Yu, S.-H.; Xiao, L.; Brock, J. D.; Zhuang, L.; Abruña, H. D. *In Situ* X-Ray Absorption Spectroscopy of a Synergistic Co–Mn Oxide Catalyst for the Oxygen Reduction Reaction. *J Am Chem Soc* **2019**, *141* (4), 1463–1466. <https://doi.org/10.1021/jacs.8b12243>.
- (69) Maurizio, C.; Habra, N. El; Rossetto, G.; Merlini, M.; Cattaruzza, E.; Pandolfo, L.; Casarin, M. XAS and GIXRD Study of Co Sites in CoAl<sub>2</sub>O<sub>4</sub> Layers Grown by MOCVD. *Chemistry of Materials* **2010**, *22* (5), 1933–1942. <https://doi.org/10.1021/cm9018106>.
- (70) Lv, H.; Song, J.; Geletii, Y. V.; Vickers, J. W.; Sumliner, J. M.; Musaev, D. G.; Kögerler, P.; Zhuk, P. F.; Bacsá, J.; Zhu, G.; Hill, C. L. An Exceptionally Fast Homogeneous Carbon-Free Cobalt-Based Water Oxidation Catalyst. *J Am Chem Soc* **2014**, *136* (26), 9268–9271. <https://doi.org/10.1021/ja5045488>.
- (71) Neel, J. V.; Schull, W. J.; McDonald, D. J.; Morton, N. E.; Kodani, M.; Takeshima, K.; Anderson, R. C.; Wood, J.; Brewer, R.; Wright, S.; Yamazaki, J.; Suzuki, M.; Kitamura, S. The Effect of Exposure to the Atomic Bombs on Pregnancy Termination in Hiroshima and Nagasaki: Preliminary Report. *Science (1979)* **1953**, *118* (3071), 537–541. <https://doi.org/10.1126/science.118.3071.537>.
- (72) K5[CoW12O40]·20H<sub>2</sub>O (K5W12CoO40[H<sub>2</sub>O]20) Crystal Structure.
- (73) Hilbrig, F.; Gobel, H. E.; Knó, H.; Schmelz, H.; Lengeler, B. *Power Generation Group KWU, Siemens AG, Otto Hahn Ring 6, 8000 München 83*; 1991; Vol. 95. <https://pubs.acs.org/sharingguidelines>.
- (74) Yamazoe, S.; Hitomi, Y.; Shishido, T.; Tanaka, T. XAFS Study of Tungsten L1- And L3-Edges: Structural Analysis of WO<sub>3</sub> Species Loaded on TiO<sub>2</sub> as a Catalyst for Photo-Oxidation of NH<sub>3</sub>. *Journal of Physical Chemistry C* **2008**, *112* (17), 6869–6879. <https://doi.org/10.1021/jp711250f>.
- (75) Weng, Z.; Wu, Y.; Wang, M.; Jiang, J.; Yang, K.; Huo, S.; Wang, X.-F.; Ma, Q.; Brudvig, G. W.; Batista, V. S.; Liang, Y.; Feng, Z.; Wang, H. Active Sites of Copper-Complex Catalytic Materials for Electrochemical Carbon Dioxide Reduction. *Nat Commun* **2018**, *9* (1), 415. <https://doi.org/10.1038/s41467-018-02819-7>.
- (76) Khemthong, P.; Photai, P.; Grisdanurak, N. Structural Properties of CuO/TiO<sub>2</sub> Nanorod in Relation to Their Catalytic Activity for Simultaneous Hydrogen Production under Solar Light. *Int J Hydrogen Energy* **2013**, *38* (36), 15992–16001. <https://doi.org/10.1016/j.ijhydene.2013.10.065>.
- (77) Gaur, A.; Shrivastava, B. D.; Joshi, S. K. Copper K-Edge XANES of Cu(I) and Cu(II) Oxide Mixtures. *J Phys Conf Ser* **2009**, *190*, 012084. <https://doi.org/10.1088/1742-6596/190/1/012084>.

- (78) Ravel, B.; Newville, M. *ATHENA*, *ARTEMIS*, *HEPHAESTUS*: Data Analysis for X-Ray Absorption Spectroscopy Using *IFEFFIT*. *J Synchrotron Radiat* **2005**, *12* (4), 537–541. <https://doi.org/10.1107/S0909049505012719>.
- (79) Sharma, A.; Varshney, M.; Park, J.; Ha, T.-K.; Chae, K.-H.; Shin, H.-J. XANES, EXAFS and Photocatalytic Investigations on Copper Oxide Nanoparticles and Nanocomposites. *RSC Adv* **2015**, *5* (28), 21762–21771. <https://doi.org/10.1039/C4RA16217J>.
- (80) Hsiao, M. C.; Wang, H. P.; Yang, Y. W. EXAFS and XANES Studies of Copper in a Solidified Fly Ash. *Environ Sci Technol* **2001**, *35* (12), 2532–2535. <https://doi.org/10.1021/es001374v>.
- (81) Abeysinghe, D.; Smith, M. D.; Yeon, J.; Tran, T. T.; Paria Sena, R.; Hadermann, J.; Halasyamani, P. S.; zur Loye, H.-C. Crystal Growth and Structure Analysis of  $Ce_{18}W_{10}O_{57}$ : A Complex Oxide Containing Tungsten in an Unusual Trigonal Prismatic Coordination Environment. *Inorg Chem* **2017**, *56* (5), 2566–2575. <https://doi.org/10.1021/acs.inorgchem.6b02710>.
- (82) Sprague-Klein, E. A.; He, X.; Mara, M. W.; Reinhart, B. J.; Lee, S.; Utschig, L. M.; Mulfort, K. L.; Chen, L. X.; Tiede, D. M. Photo-Electrochemical Effect in the Amorphous Cobalt Oxide Water Oxidation Catalyst Cobalt-Phosphate (CoPi). *ACS Energy Lett* **2022**, *7* (9), 3129–3138. <https://doi.org/10.1021/acsenenergylett.2c01560>.
- (83) Hunault, M.; Vercamer, V.; Haverkort, M. W.; Arrio, M.-A.; Brouder, C.; Calas, G.; Juhin, A. Tracking the Signature of Low Symmetry Environments in the XAS *K* Pre-Edge. *J Phys Conf Ser* **2016**, *712*, 012005. <https://doi.org/10.1088/1742-6596/712/1/012005>.
- (84) Esmailirad, M.; Kondori, A.; Song, B.; Ruiz Belmonte, A.; Wei, J.; Kucuk, K.; Khanvilkar, S. M.; Efimoff, E.; Chen, W.; Segre, C. U.; Shahbazian-Yassar, R.; Asadi, M. Oxygen Functionalized Copper Nanoparticles for Solar-Driven Conversion of Carbon Dioxide to Methane. *ACS Nano* **2020**, *14* (2), 2099–2108. <https://doi.org/10.1021/acsnano.9b08792>.
- (85) Frenkel, A. I.; Hills, C. W.; Nuzzo, R. G. A View from the Inside: Complexity in the Atomic Scale Ordering of Supported Metal Nanoparticles. *J Phys Chem B* **2001**, *105* (51), 12689–12703. <https://doi.org/10.1021/jp012769j>.
- (86) Frenkel, A. Solving the 3D Structure of Metal Nanoparticles. *Z Kristallogr Cryst Mater* **2007**, *222* (11), 605–611. <https://doi.org/10.1524/zkri.2007.222.11.605>.
- (87) Clausena, B. S.; Topsøe, H.; Hansen, L. B.; Stoltze, P.; Nørskov, J. K. Determination of Metal Particle Sizes from EXAFS. *Catal Today* **1994**, *21* (1), 49–55. [https://doi.org/10.1016/0920-5861\(94\)80033-2](https://doi.org/10.1016/0920-5861(94)80033-2).
- (88) Durst, J.; Siebel, A.; Simon, C.; Hasché, F.; Herranz, J.; Gasteiger, H. A. New Insights into the Electrochemical Hydrogen Oxidation and Evolution Reaction Mechanism. *Energy Environ. Sci.* **2014**, *7* (7), 2255–2260. <https://doi.org/10.1039/C4EE00440J>.
- (89) Sheng, W.; Zhuang, Z.; Gao, M.; Zheng, J.; Chen, J. G.; Yan, Y. Correlating Hydrogen Oxidation and Evolution Activity on Platinum at Different pH with Measured Hydrogen Binding Energy. *Nat Commun* **2015**, *6* (1), 5848. <https://doi.org/10.1038/ncomms6848>.
- (90) Anantharaj, S.; Noda, S.; Jothi, V. R.; Yi, S.; Driess, M.; Menezes, P. W. Strategies and Perspectives to Catch the Missing Pieces in Energy-Efficient Hydrogen Evolution Reaction in Alkaline Media. *Angewandte Chemie International Edition* **2021**, *60* (35), 18981–19006. <https://doi.org/10.1002/anie.202015738>.
- (91) Huang, C.; Sasaki, K.; Senthil Raja, D.; Hsieh, C.; Wu, Y.; Su, J.; Cheng, C.; Cheng, P.; Lin, S.; Choi, Y.; Lu, S. Twinning Enhances Efficiencies of Metallic Catalysts toward Electrolytic Water Splitting. *Adv Energy Mater* **2021**, *11* (46). <https://doi.org/10.1002/aenm.202101827>.
- (92) Ye, L.; Wen, Z. Self-Supported Three-Dimensional Cu/Cu<sub>2</sub>O–CuO/RGO Nanowire Array Electrodes for an Efficient Hydrogen Evolution Reaction. *Chemical Communications* **2018**, *54* (49), 6388–6391. <https://doi.org/10.1039/C8CC02510J>.
- (93) Putra, R. P.; Horino, H.; Rzeznicka, I. I. An Efficient Electrocatalyst for Oxygen Evolution Reaction in Alkaline Solutions Derived from a Copper Chelate Polymer via In Situ Electrochemical Transformation. *Catalysts* **2020**, *10* (2), 233. <https://doi.org/10.3390/catal10020233>.
- (94) Kumar, B.; Saha, S.; Ojha, K.; Ganguli, A. K. A Facile One Step Synthesis of Cu/Cu<sub>2</sub>O Nanocomposites: Enhanced Hydrogen/Oxygen Evolution. *Mater Res Bull* **2015**, *64*, 283–287. <https://doi.org/10.1016/j.materresbull.2014.10.076>.
- (95) Yang, H.; Gao, S.; Rao, D.; Zhang, C.; Zhou, X.; Yang, S.; Ye, J.; Yang, S.; Lai, F.; Yan, X. Non-Metallic Electronic Regulation in CuCo Oxy-/Thio-Spinel as Advanced Oxygen Evolution Electrocatalysts. *Sci China Chem* **2021**, *64* (1), 101–108. <https://doi.org/10.1007/s11426-020-9895-2>.
- (96) Chauhan, M.; Reddy, K. P.; Gopinath, C. S.; Deka, S. Copper Cobalt Sulfide Nanosheets Realizing a Promising Electrocatalytic Oxygen Evolution Reaction. *ACS Catal* **2017**, *7* (9), 5871–5879. <https://doi.org/10.1021/acscatal.7b01831>.
- (97) Babar, P. T.; Lokhande, A. C.; Pawar, B. S.; Gang, M. G.; Jo, E.; Go, C.; Suryawanshi, M. P.; Pawar, S. M.; Kim, J. H. Electrocatalytic Performance Evaluation of Cobalt Hydroxide and Cobalt Oxide Thin Films for Oxygen Evolution Reaction. *Appl Surf Sci* **2018**, *427*, 253–259. <https://doi.org/10.1016/j.apsusc.2017.07.142>.



For Table of Contents Only.